Unraveling the importance of controlled architecture in bimetallic multilayer electrode toward efficient electrocatalyst

Minsu Gu[a], Byeong-Su Kim[a,b,*]

[a] Department of Energy Engineering, Ulsan National Institute of Science and Technology (UNIST), Ulsan 44919, South Korea
[b] Department of Chemistry, Ulsan National Institute of Science and Technology (UNIST), Ulsan 44919, South Korea

ABSTRACT

Even though traditional electrode fabrication methods such as simple mixing process have been used in various energy storage and conversion devices due to its handiness, these methods could not fully utilize and maximize the intrinsic properties of each active material. With the limited control over the internal structure of the electrode, it also often poses a significant challenge to elucidate the structure-property relationship between components within the electrode. Taking advantages of versatile layer-by-layer (LbL) assembly which can tailor nano-architecture of hybrid electrodes, here we report electrocatalytic thin films for methanol oxidation by adjusting the assembly sequence of LbL films composed of the Au and Pd nanoparticles (NPs) and graphene oxide (GO) nanosheets. In case of co-assembled bimetallic LbL structure of $(GO/Au/GO/Pd)_n$ where respective Au and Pd NPs are supported with GO nanosheets, the electrocatalytic activity is significantly higher than that of respective monometallic LbL electrode (i.e. $(GO/Au)_n$, and $(GO/Pd)_n$). To further investigate the architecture effect on the electrochemical behavior, Au and Pd NPs are assembled with GO in a different relative position of hybrid multilayer electrodes. It is proved that the electrocatalytic activity can be highly tunable by the position of metal NPs in the LbL structure, suggesting the structural dependence of charge and mass transfer between the electrolyte and the electrode, which is otherwise impossible to investigate in a simple conventional electrode fabrication method. Because of the highly tunable properties of LbL assembled electrodes coupled with electrocatalytic NPs, we anticipate that the general concept presented here will offer new insights in the nanoscale control over the architecture of the electrode toward development of novel electroactive catalysts.

1. Introduction

The rapid depletion of fossil fuels and growing environmental concerns have created an enormous worldwide demand for alternative technologies of clean and renewable energies [1,2]. Therefore, there have been significant researches for electrochemical energy conversion technology, as following that the design of electrodes with high conversion efficiency becomes very important. Typically, various electroactive materials with conductive supports are fabricated into electrodes of energy conversion devices by simple mixing process [3]; however, these traditional electrode fabrication methods not only could not fully utilize the intrinsic properties of each active material, but also limit analyzing the contribution of individual materials to the overall performance of the electrode. For this reason, a more concerted approach to fabricate the nanostructured electrode with a fine structural control is gaining more attention [4,5].

Among many assembly strategies for these nanostructured electrode with two or more components, layer-by-layer (LbL) assembly is one of the most versatile nanoscale blending methods to assemble diverse materials on various surfaces [6–10]. The LbL assembly is often achieved through the sequential adsorption of materials with complementary functional groups employing electrostatic interactions, hydrogen bonding, or other intermolecular interactions [11,12]. Thus, highly ordered multilayered architectures can be manufactured reproducibly, allowing nanoscale-level control over both composition and structure of hybrid multilayers with the choice of materials and sequence of layering. With these unique opportunities, there are active researches on LbL assembled thin films for various energy storage and conversion applications, including lithium ion battery, supercapacitor, fuel cell, solar cell and electrocatalyst [13–19]. Along with the development of hybrid electrodes, there have been approaches, including our own, to couple unique physical and chemical properties of 2-dimensional (2D) nanomaterials such as graphene nanosheets with the versatility of LbL assembly for electronic and biomaterial surfaces [20–31]; for example, we found that the graphene oxide (GO) nanosheets not only serve as a structural component of the multilayer thin films,
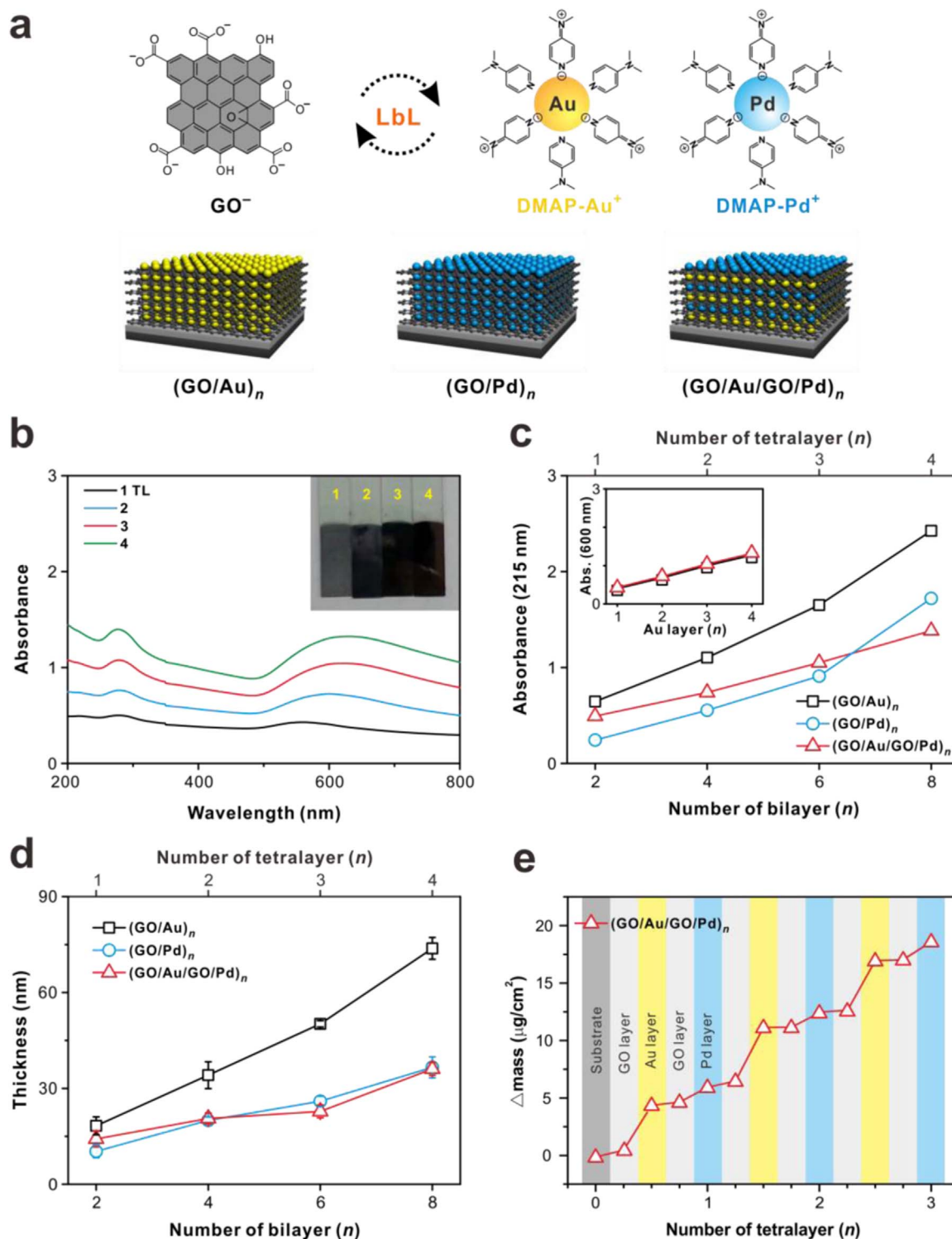
Fig. 1. Films growth characteristics of LbL assembled multilayer electrodes. (a) Schematic representation of layer-by-layer (LbL) assembled monometallic $(GO/Au)_n$, and $(GO/Pd)_n$ and bimetallic $(GO/Au/GO/Pd)_n$ multilayer thin films for methanol oxidation reaction. (b) UV/vis absorbance spectra of $(GO/Au/GO/Pd)_n$ multilayer thin films. Inset image represents the samples prepared. (c) The corresponding absorbance maxima of multilayer films at 215 nm with $(GO/Au)_n$ and $(GO/Pd)_n$. Inset represents the corresponding absorbance maxima of multilayer films at 600 nm. (d) The thickness of each film measured by a surface profiler. (e) Mass change by QCM analysis as a function of the number of tetralayer of $(GO/Au/GO/Pd)_n$ multilayer thin films.

but also potentially improve the utilization of metal NPs within the electrode, emphasizing the critical role of graphene as a chemically stable support in preserving the catalytic active surface of Au NPs [18]. It is also interesting to observe that the electrocatalytic activity of hybrid electrode is highly tunable with respect to the number of layers. Onda et al. have previously reported the importance of well-organized

layered structures with different performance through sequential reaction in the design of multi-enzyme reactors using glucose oxidase and glucoamylase as biocatalysts [32]. However, there is no report on the investigation of electrochemical activity of multilayer electrode and the associated electrochemical communication between active materials with respect to the internal architecture (i.e. controlled by layering

sequence) when more than two active components are involved.

In that regard, herein we report the creation of 3D hybrid electrocatalytic thin films with varying internal architectures that are composed of two electroactive Au and Pd NPs integrated with graphene nanosheets with LbL assembly. In specific, we focused on the elucidation of architecture-property relationship of hybrid electrodes toward methanol oxidation reaction (MOR) as a model electrocatalytic reaction (Fig. 1a).

We found that the electrocatalytic activity is highly tunable by the number and the position of metal NPs in the LbL structure, suggesting the considerable structural dependence of mass transfer of the electrolyte within the 3D hybrid electrode. Moreover, even with the identical composition of constituent NPs, the hybrid electrode exhibited highly tunable electrocatalytic activity depending on the electrode architecture, which is otherwise impossible to investigate with a simple electrode fabrication method. Considering the versatile nature of LbL assembly coupled with electroactive NPs, the approach developed here will offer new insights in the design of the nanoscale electrodes for advanced energy conversion devices.

2. Experimental

2.1. Preparation of GO

Graphite oxide was synthesized from graphite powder (Sigma-Aldrich) by modified Hummers method and exfoliated to give a brown dispersion of graphene oxide (GO) under ultrasonication at a concentration of 0.50 mg/mL [33,34].

2.2. Preparation of Au and Pd NPs

The 4-(dimethylamino)pyridine (DMAP)-stabilized Au and Pd NPs were prepared by using the spontaneous phase transfer from organic solvent according to a literature method [35].

2.3. Layer-by-layer assembly of hybrid electrode films

ITO-coated glass substrate was cleaned by sonication in deionized (DI) water, acetone and ethanol for 10 min. Silicon and quartz substrates were cleaned by piranha solution to remove any organic contamination and subsequently treated with (3-aminopropyl)triethoxysilane to introduce positively charged hydrophilic surface. These substrates were first dipped into negatively charged GO solution (0.50 mg/mL) at pH 4 for 10 min. It was then dipped into DI water for 1 min three times to remove loosely bound GO. Subsequently, the substrate was then dipped into positively charged DMAP-coated Au or Pd NPs suspension at pH 11 for 10 min, and washed with DI water three times for 1 min, which afforded one-bilayer film of $(GO/Au)_1$ or $(GO/Pd)_1$, respectively. The above procedures were repeated to achieve the desired number of bilayers (n). Multicomponent assembly was conducted using the identical procedure with both Au and Pd NP suspensions. All as-assembled multilayer films were subjected to thermal reduction at 150 ºC for 12 h in an oven. For comparison, a commercial 30 wt% palladium nanoparticles supported by carbon black (Pd/C, Sigma-Aldrich) was used as a control. Pd/C ink was prepared by dispersing 20 mg of Pd/C powder in 2.0 mL of DI water and 40 μL of 5 wt% Nafion solution (Sigma-Aldrich). 5 μL of the Pd/C ink was dropped on a glassy carbon electrode (diameter: 3 mm).

2.4. Electrochemical analysis

Electrochemical experiments were performed using a standard three electrode cell configuration (Biologic science instrument, VSP). A platinum wire was used as a counter electrode and Hg/HgO as a reference. The working electrode was multilayer thin film assembled on ITO-coated glass. Cyclic voltammetry (CV) was performed between

−0.60 and 0.60 V in 0.10 M KOH solution with 1.0 M methanol solution at room temperature in a saturated N_2 at a scan rate of 20 mV s^{-1}. The current density was calculated by dividing the geometric area (cm^2) of as-prepared LbL electrodes. The values of potential were converted from versus Hg/HgO to versus the reversible hydrogen electrode (RHE) by: Hg/HgO +0.879 V = RHE. For the correction, the potential difference between Hg/HgO and RHE was measured in a cell where platinum wires were used as the working and counter electrodes in a H_2-saturated aqueous electrolyte of 0.10 M KOH with Hg/HgO as the reference electrode (Fig. S1 in the Supporting Information). Linear sweep voltammetry (LSV) was carried out at a scan rate of 5 mV s^{-1}. Electrochemical impedance spectroscopy (EIS) measurements were carried out in the frequency range from 100 kHz to 100 mHz under AC stimulus of 10 mV in amplitude.

2.5. Characterizations

The absorbance of the thin films was characterized by using UV/vis spectroscopy (VARIAN, Cary 5000). The thickness of the as-prepared samples on silicon substrates was measured by surface profiler (KLA Tencor, P-6). The surface morphology of the samples was investigated using scanning electron microscopy (Cold FE-SEM, Hitachi, S-4800) and atomic force microscopy (AFM, Nanoscope V, Veeco) via a tapping mode. The size and morphology of the prepared NPs were measured by transmission electron microscopy (Normal-TEM, JEOL, JEM-2100, accelerating voltage of 200 kV). The LbL films were analyzed by X-ray photoelectron spectroscopy (XPS, Thermo Fisher, K-alpha). The cross-sectional TEM samples were prepared by focus ion beam (FIB) technique (FEI, Quanta 3D FEG) and the cross-sectional images were obtained by high-resolution transmission electron microscopy (HR-TEM), high-angle annular dark field scanning transmission electron microscopy (HAADF-STEM), and energy dispersive X-ray spectroscopy (EDXS) (JEOL, JEM-2100F, accelerating voltage of 200 kV). The active mass of each material adsorbed onto the film surface was analyzed by a quartz crystal microbalance (QCM, Stanford Research System, QCM200), using the following Sauerbrey Eq. (1) and (2):

$$\Delta F \,(\text{Hz}) = -\frac{2F_o^2}{A\sqrt{\rho_q \mu_q}}\Delta m \tag{1}$$

$$\Delta F \,(\text{Hz}) = -56.6 \times \Delta m \tag{2}$$

where ΔF is the resonant frequency change (Hz), Δm is the mass change per unit area of the quartz crystal (μg/cm^2), F_o (5 MHz) is the fundamental resonance frequency of the crystal, A is the area of the Au-Cr electrode, ρ_q (2.65 g cm^{-3}) is the density of quartz crystal and μ_q (2.95×10^{11} g cm^{-1} s^{-2}) is the shear modulus. Consequently, the specific current was calculated by dividing the peak current by the active mass of metal NPs.

3. Results and discussion

3.1. Fabrication of hybrid LbL electrodes

Highly stable aqueous suspensions of GO and the electrocatalytic metal NPs are necessary to fabricate 3D LbL assembled electrocatalyst films. Negatively charged GO suspension possessing many oxygen-containing functional groups such as carboxyl acids, hydroxyl, and epoxide groups was initially prepared using the modified Hummers method [33,34]. Subsequently, positively charged Au and Pd NPs were prepared by using the spontaneous phase transfer from organic solvent with 4-(dimethylamino)pyridine (DMAP) ligand [35]. We employed the identical ligand for the synthesis of both NPs to minimize the ligand effect on the electrocatalytic activity. The average diameter of Au and Pd NPs was determined to be 5.8 nm and 3.4 nm (see Fig. S2 in the Supporting information). With these stable suspensions of the positively charged NPs as electroactive species and the negatively charged

GO as a stable support, we fabricated three types of multilayer films by LbL assembly onto a silicon wafer, quartz and ITO-coated glass slide, respectively. In specific, homogeneous monometallic hybrid electrodes consisting of GO and respective metal NPs (either Au or Pd NPs) were assembled in an architecture of substrate/$(GO/Au)_n$ or substrate/$(GO/Pd)_n$ (n = number of bilayer (BL), typically n =2–8). Moreover, heterogeneous bimetallic electrodes composed of GO and both metal NPs were assembled in the format of substrate/$(GO/Au/GO/Pd)_n$ (n = number of tetralayer (TL), typically n =1–4).

The successful growth of each multilayer was monitored by the gradual increase of absorbance upon increasing the number of layers in UV/vis spectra (Fig. 1b and see Fig. S3 in the Supporting information). The linear growth curve corresponding absorbance maxima of GO at 215 nm clearly demonstrates the uniform multilayer formation after each assembly (Fig. 1c). Interestingly, we found that the absorbance sum of each $(GO/Au)_n$ and $(GO/Pd)_n$ multilayer was similar to that of bimetallic $(GO/Au/GO/Pd)_n$ films, suggesting the precise control over the thickness and composition of multilayers without significantly altering the internal structures. In other case, the surface plasmon absorbance of Au NPs at 600 nm within heterostructured $(GO/Au/GO/Pd)_n$ was matching exactly to that of Au NPs within $(GO/Au)_n$ multilayer films (inset in Fig. 1c). Despite two different NPs are alternatively deposited within $(GO/Au/GO/Pd)_n$ multilayer, it is interesting to observe that the amount of Au NPs is constant with the $(GO/Au)_n$ multilayer films owing to the identical charge density of Au NPs. The corresponding thickness of each multilayer film shows a linear growth with respect to the number of deposition steps with an average bilayer thickness corresponding to 8.82 nm, 4.77 nm for a single bilayer of $(GO/Au)_n$ and $(GO/Pd)_n$ multilayer, respectively, and 14.2 nm for a single tetralayer of $(GO/Au/GO/Pd)_n$ films (Fig. 1c). The average thickness of a single tetralayer is in accord with the sum of the average bilayer thickness of two monometallic films, which demonstrates the high fidelity of the LbL assembly in building hybrid electrodes.

We further analyzed the adsorption behavior of GO, Au and Pd NPs in $(GO/Au/GO/Pd)_n$ multilayer films using a quartz crystal microbalance (QCM). Fig. 1e shows the stepwise measurement of the mass deposited after each layer, indicating the amount of each component in the multilayer structure quantitatively; for example, the average mass was found to be 0.55 µg/cm², 4.31 µg/cm² and 1.38 µg/cm² for GO, Au and Pd NPs, respectively, within a single tetralayer. The adsorption of metal NPs was the higher than that of GO sheets, implying that it would be advantageous in respect to catalytic effect on metal by high mass loading per unit area. In addition, the amount of Au NPs was higher than that of Pd NPs, resulting in accord with the growth curves in UV/vis spectra and thickness data.

3.2. Effect of co-assembly of Au and Pd NPs

As we found that the thermally treated multilayer films at 150 °C exhibited superior electrocatalytic activity for methanol oxidation in our previous study, each multilayer film underwent the thermal reduction process before investigating the electrochemical characteristics. Thermal reduction not only restores the electrical conductivity of GO, but also eliminates the excess DMAP ligands, which would prevent the effective electrocatalytic reaction on the surfaces of Au and Pd NPs. However, the thermal treatment higher than 150 °C for further reduction of GO did not improve the electrocatalytic activity toward the methanol oxidation significantly, suggesting the ligand mobility atop Au NPs is more critical in enhancing the overall electrocatalytic activity [18].

The anodic peak potential of Pd NPs was observed at around 0 V and the current density of $(GO/Pd)_n$ multilayer films showed the highest value of 3.45 mA/cm² at 6 BL at 0.01 V which is approximately 6 times higher than that of $(GO/Au)_6$ multilayer films (0.54 mA/cm²). This result indicates the methanol oxidation on Pd NPs is more

effective than on Au NPs in alkaline electrolyte as known in the previous literatures [36,37]. It is of note that the peak current (i_p) increased gradually due to the increased concentration of active Pd NPs upon LbL assembly with electrochemical surface areas (ECSAs) (Fig. S4 in the Supporting information), which then decreased after the 6 BL as similarly observed in $(GO/Au)_n$ multilayers [18]. The decreased peak current above 6 BL is explained due to the limited diffusion of methanol into the 3D electrode as related to the layered architecture of GO nanosheets. The barrier effect of 2D GO sheets in the multilayer film was demonstrated similarly in gas barrier film [38].

To evaluate this commonly observed phenomenon in LbL electrode, logarithmic current with respect to various scan rates (v) was plotted to calculate an exponent of scan rate, which represents a transfer mechanism governed by a diffusion-limited mass transfer and a surface-confined charge transfer process (Fig. S5 in the Supporting information) [39]. In an ultrathin layer system where only adsorbed electroactive species react on the surface of film irreversibly, the peak current (i_p) is given as follows in Eq. (3):

$$i_p = \frac{\alpha F^2 A v \Gamma_O^*}{2.718RT} \tag{3}$$

where α is the transfer coefficient, F is the Faraday constant (C/mol), v is the scan rate (V/s), A is the area (cm²), Γ_O^* is the amount of electroactive components (mol/cm²), R is the ideal gas constant (J/K·mol), and T is the temperature (K). This relation reveals that the peak current density is directly proportional to v. As increasing the films thickness, however, the mass transfer from electrolyte becomes a limiting factor and the peak current (i_p) is given as follows in Eq. (4):

$$i_p = FAC_O^* D_O^{1/2} v^{1/2} \left(\frac{\alpha F}{RT}\right)^{1/2} \pi^{1/2} \chi(bt) \tag{4}$$

where D_O is the diffusion coefficient (cm²/s), $\chi(bt)$ is a function for the normalized current for irreversible system, and C_O^* is the bulk concentration of electroactive components (mol/cm³). According to this relationship, the peak current is proportional to $v^{1/2}$. Based on these electrochemical kinetics on electrode, the slope was gradually decreased from 0.71 to 0.60 as increasing the number of bilayer, indicating electrochemical behavior in LbL assembled electrode changed from surface-confined to diffusion-limited process. In a separate study, Lutkenhaus group reported that the shift was caused by a transition from a surface-confined process to a diffusion-limited process within the LbL assembled electrode of polyaniline / vanadium pentoxide [40]. Eventually, a balance between mass and charge transfer at 6 BL was optimized, leading to the observed electrocatalytic behavior.

On the basis of maximum catalytic effect of monometallic system at 6 BL film through a fine balance between the methanol diffusion and electron transfer process, we evaluated the catalytic effect of bimetallic system, where both Au and Pd NPs are alternatively assembled within heterogeneous $(GO/Au/GO/Pd)_3$ films (Fig. 2b). As a control, we also prepared individual $(GO/Au)_3$ and $(GO/Pd)_3$ monometallic electrodes. The successful fabrication of co-assembled bimetallic electrode was also monitored by the presence of respective Au 4 f and Pd 3d signals in $(GO/Au/GO/Pd)_3$ films comparing to respective monometallic $(GO/Au)_3$ and $(GO/Pd)_3$ electrodes in high-resolution X-ray photoelectron spectroscopy (XPS) (see Fig. S6 in the Supporting information). To our surprise, the peak current (i_p) of co-assembled bimetallic $(GO/Au/GO/Pd)_3$ films at 0.34 V increased to 10.3 mA/cm², significantly higher than 0.20 mA/cm² and 1.22 mA/cm² of individual monometallic $(GO/Au)_3$ and $(GO/Pd)_3$ electrode, respectively. It is also of note that the co-assembled bimetallic $(GO/Au/GO/Pd)_3$ electrode exhibits three times higher peak current than that of $(GO/Pd)_6$ film even at a lower content of Pd NPs. This observation clearly suggests that there exists a synergistic effect on the enhancement of electrocatalytic effect within heterogeneous bimetallic 3D multilayer electrode. In addition, the
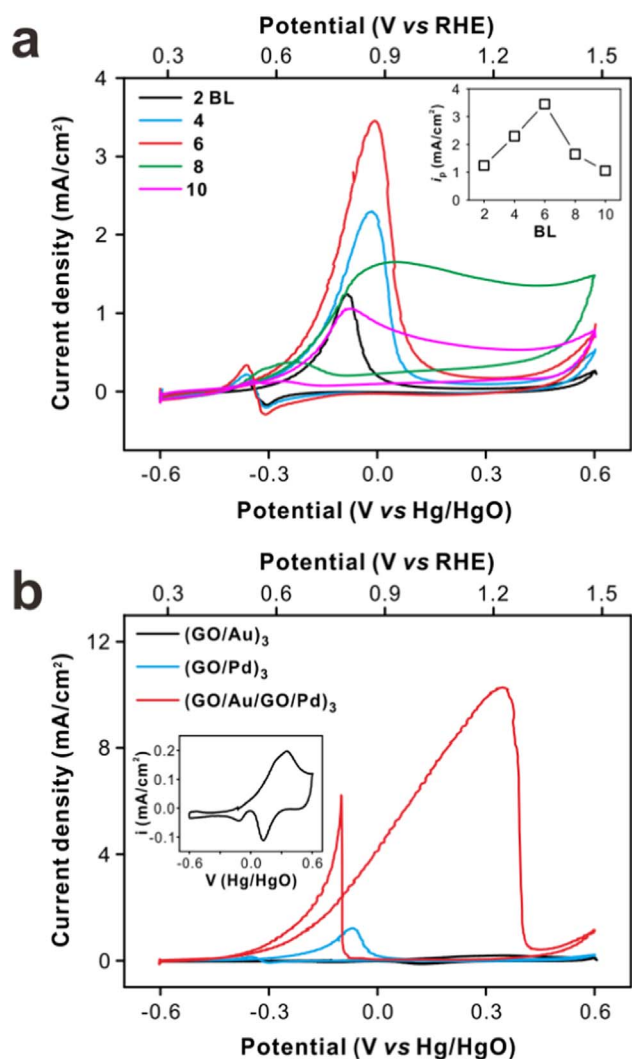
Fig. 2. Catalytic effect for methanol oxidation reaction. Cyclic voltammograms (CVs) of (a) $(GO/Pd)_n$ multilayer thin films with an inset of the current density plot as a function of number of bilayer (BL) in $(GO/Pd)_n$ multilayer films. (b) Comparison of electrocatalytic activity of $(GO/Au)_3$, $(GO/Pd)_3$ and $(GO/Au/GO/Pd)_3$ films. Inset in Fig. 2b shows a magnified CV of $(GO/Au)_3$. All measurements were performed in 0.10 M KOH with 1.0 M CH_3OH in a saturated N_2 at a scan rate of 20 mV s^{-1}.

electrocatalytic activity of $(GO/Au/GO/Pd)_3$ film did not alter when the sequence of layering is reversed as in $(GO/Pd/GO/Au)_3$ films (Fig. S7 in the Supporting information).

Furthermore, as a long-term stability is a critical requirement in development of efficient electrocatalyst, we performed a stability test of $(GO/Au/GO/Pd)_3$ electrode through multiple electrocatalytic cycles (Fig. S8 in the Supporting Information). The anodic peak current continuously increased initially from first to 30th cycles, which then followed by a slight decrease afterwards. The increase in initial cycling was due to full activation for diffusion of methanol molecules into undermost layer from interface of electrolyte and the 3D electrode, in accordance with other report employing porous graphene aerogel electrode [41]. Bimetallic $(GO/Au/GO/Pd)_3$ hybrid film exhibited a superior electrochemical stability over 100 cycles with a retention of 90%, owing to the stable graphene sheets support for electroactive metal NPs as well as the improved electron pathway within 3D interconnected LbL films. Another source of the improved cyclic stability is the interplay of Au and Pd NPs, as demonstrated in the poor cycle retention of only 5% of $(GO/Pd)_6$ film over 100 cycles. It is known that Au NP displays a poisoning tolerance for byproduct during MOR such as CO through further oxidation of the CO [42,43]. As a

result, Au NPs can provide sites to Pd NPs for effective MOR by regenerating contaminated metal surface through CO removal.

3.3. Effect of LbL architecture

Until now, we investigated highly improved catalytic effect by co-assembly with Au and Pd NPs and the conversion of electrochemical operating principles above certain layer thickness. We then examined the impact of the electrode architecture on the electrochemical behavior of hybrid films more in detail, such that the role of GO within the multilayer in controlling the diffusion pathways as well as the influence of relative position of metal NPs in terms of tailoring the electrochemical reactions because adsorbates such as methanol molecules from electrolyte are more accessible to surface of electrode. Thus, we fabricated three types of multilayer films using different sequence of layering to afford 3D hybrid electrodes of varying architecture (Fig. 3): fully alternating Au and Pd NPs, $(GO/Au/GO/Pd)_3$, Pd layered on top of Au NPs, $(GO/Au)_3/(GO/Pd)_3$, and Au layered over Pd NPs, $(GO/Pd)_3/(GO/Au)_3$, respectively. The location of the NPs within the multilayer electrode was determined in consideration of balance between electrode (inner-layer) and electrolyte (outer-layer). In addition, all electrodes were fixed at 6 BL due to the optimized balance of mass and charge transfer as studied in a previous section. It is worth noting that the precision in engineering the architecture of electrode can be achieved simple by changing the sequence of the deposition steps during the assembly, highlighting the versatile nature of the LbL assembly in building the 3D electrode.

The successful fabrication of respective 3D electrodes is confirmed by cross-sectional high-resolution transmission electron microscopy (TEM) (Fig. 3). The multilayer films of different architectures are clearly observed with the aid of the contrast difference between Au and Pd NPs (see also Fig. S2 in the Supporting information). The junction between GO and NPs is also demonstrated with a distinct morphology of graphene sheet within the layers (Fig. S9 in the Supporting information). Furthermore, the associated elemental information within the hybrid electrode was elucidated by high-angle annular dark field scanning transmission electron microscopy (HAADF-STEM). The HAADF-STEM images indicate the homogeneous lateral distribution of each corresponding element within LbL films. As shown in Fig. 3a, Au and Pd NPs were distributed in the entire films of $(GO/Au/GO/Pd)_3$, whereas each NPs are localized in the respective position in the separated films of $(GO/Au)_3/(GO/Pd)_3$ and $(GO/Pd)_3/(GO/Au)_3$ (Fig. 3b and c); however, it is also of note that the interlayer diffusion of the smaller Pd NPs within the multilayer is also observed as often demonstrated in some LbL systems [44,45].

The analysis of the surfaces of each film also supports the hierarchically assembled films. According to the atomic force microscopy (AFM) images, surface root-mean-square roughness (R_{rms}) values (averaged over 10×10 μm^2) of $(GO/Au/GO/Pd)_3$, $(GO/Au)_3/(GO/Pd)_3$ and $(GO/Pd)_3/(GO/Au)_3$ films were determined to be 6.05, 5.31 and 9.48 nm, respectively (Fig. S10 in the Supporting information). When Au NPs are deposited on outer-layers of films, the surface roughness increases because the size of Au NPs is larger than that of Pd NPs. In contrast, the films terminating with smaller sized Pd NPs display smoother morphology in general. Additionally, the scanning electron microscopy (SEM) images illustrate the successful deposition of Au and Pd NPs on top of the GO sheets (Fig. S11 in the Supporting information).

3.4. Electrocatalytic activity of hybrid LbL electrodes

The electrochemical measurements were carried out to investigate the influence of electrode architecture on the electrochemical performance toward MOR. Besides the heterostructured $(GO/Au)_3/(GO/Pd)_3$, $(GO/Pd)_3/(GO/Au)_3$ and $(GO/Au/GO/Pd)_3$ multilayer films with different structures, respective homogeneous $(GO/Au)_3$ and $(GO/Pd)_3$
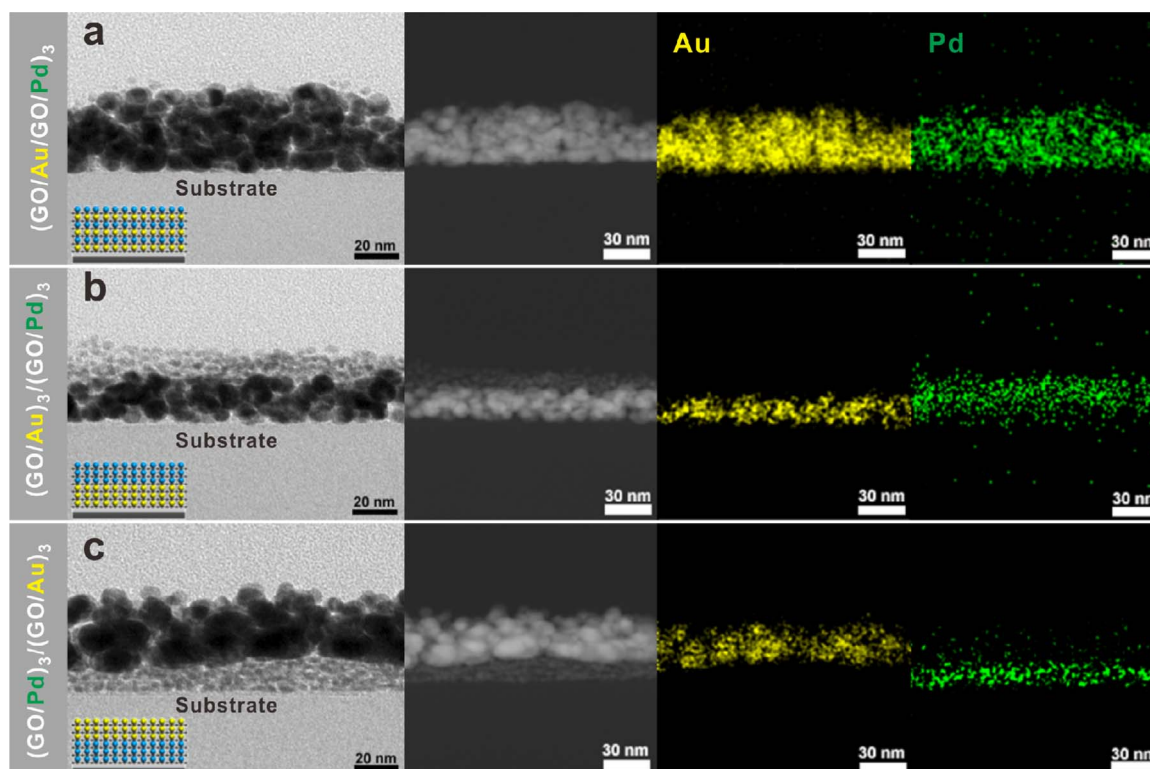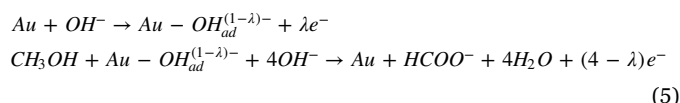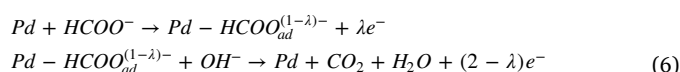
Fig. 3. Architecture controlled multilayer thin films. Representative cross-sectional high-resolution TEM and HAADF-STEM images with composed elemental mapping images of Au and Pd of (a) (GO/Au/GO/Pd)$_3$, (b) (GO/Au)$_3$/(GO/Pd)$_3$ and (c) (GO/Pd)$_3$/(GO/Au)$_3$ multilayer thin films.

multilayers were assembled for comparison (Fig. 4a). As shown in Fig. 2, all of Au and Pd NPs co-assembled bimetallic electrodes showed remarkably increased peak current values comparing to control sets of monometallic (GO/Au)$_3$ and (GO/Pd)$_3$ multilayer films. However, most interestingly, there was a definite difference of electrochemical activity between hybrid films of opposite sequence of layering such as (GO/Au)$_3$/(GO/Pd)$_3$ and (GO/Pd)$_3$/(GO/Au)$_3$. For example, the anodic peak current of (GO/Pd)$_3$/(GO/Au)$_3$ (10.3 mA/cm^2) is approximately 1.7 times higher than that of (GO/Au)$_3$/(GO/Pd)$_3$ (5.9 mA/cm^2). This difference clearly demonstrates that the structural difference on 3D electrode significantly influences on the electrochemical catalytic effect by the surface reaction.

In order to elucidate the origin of this structural effect on the kinetics of heterogeneous multilayer films, the Tafel plot of each electrode was displayed (Fig. 4b). The Tafel region of (GO/Au)$_n$ and (GO/Pd)$_n$, following a negligible mass transfer process, is limited by charge transfer for the dissociation of methanol by C-H bond breaking. This region has distinct linear ranges from 0 to 0.25 V (yellow region in Fig. 4b) and from −0.35 to −0.10 V (blue region in Fig. 4b) with a Tafel slope of 311 and 192 mV/dec, respectively. The lower Tafel slope of (GO/Pd)$_n$ indicates the faster kinetics than (GO/Au)$_n$ during MOR, resulting the higher anodic peak current in applied potential as shown in Fig. 2b. The non-linear Tafel region in the potential range from 0 to 0.25 V of (GO/Pd)$_n$ films indicates that mass transfer limited system begins to dominate due to high overpotential to overcome the restricted charge transfer. In bimetallic electrode, therefore, each rate-determining step of MOR is overlapped between mass transfer limited system by (GO/Pd)$_n$ and charge transfer limited system by (GO/Au)$_n$ films in potential window from 0 to 0.25 V, and the whole kinetics of bimetallic multilayer films is affected as which metal NPs are outer-layered because of the concentration gradient of reactants in 3D electrode by different electrochemical kinetics. Generally, methanol oxidation is catalyzed on Au NPs with the adsorption of OH$^-$ (OH$^-_{ad}$) in alkaline media by the following reactions (5), where the charge transfer coefficient λ varies between 0 and 1 [18]:

$$Au + OH^- \rightarrow Au - OH^{(1-\lambda)-}_{ad} + \lambda e^-$$
$$CH_3OH + Au - OH^{(1-\lambda)-}_{ad} + 4OH^- \rightarrow Au + HCOO^- + 4H_2O + (4-\lambda)e^-$$
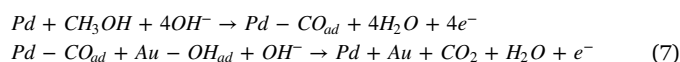$$(5)$$

The formate species produced on Au NPs can then serve as a reactive intermediate on Pd NPs with the concomitant adsorption of formate (HCOO$^-_{ad}$) in alkaline media by following reactions (6) [36]:

$$Pd + HCOO^- \rightarrow Pd - HCOO^{(1-\lambda)-}_{ad} + \lambda e^-$$
$$Pd - HCOO^{(1-\lambda)-}_{ad} + OH^- \rightarrow Pd + CO_2 + H_2O + (2-\lambda)e^- \quad (6)$$

In other words, Au NPs can supply additional reactant to Pd NPs, resulting in the enhanced mass transfer by alleviating the reactant depletion in 3D electrode. Therefore, when Au NPs are located in the outer-layer of hybrid films, such as (GO/Pd)$_3$/(GO/Au)$_3$, it displayed the higher current density by a larger overpotential applied until 0.4 V due to the enhanced mass transfer into inner-layered Pd NPs. On the other hand, when Pd NPs are located in outer-layer of multilayer film, such as (GO/Au)$_3$/(GO/Pd)$_3$, oxidation rate on Au NPs is limited by mass transfer due to methanol depletion via outer-layered Pd NPs although the current density was increased until 0.16 V by supplying a small amount of formate from inner-layered Au NPs (Scheme 1).

The improved catalytic activity of the primary active metal Pd in the presence of adsorbed OH (OH$_{ad}$) on the secondary metal Au has been commonly explained by a bifunctional mechanism via the Langmuir-Hinshelwood (L-H) pathway (7) [42]:

$$Pd + CH_3OH + 4OH^- \rightarrow Pd - CO_{ad} + 4H_2O + 4e^-$$
$$Pd - CO_{ad} + Au - OH_{ad} + OH^- \rightarrow Pd + Au + CO_2 + H_2O + e^- \quad (7)$$

It is recently reported that Ni(OH)$_2$ can facilitate the oxidative removal of carbonaceous poisons from adjacent Pt sites by supplying sufficient OH$_{ad}$ through L-H pathway [46]. This bifunctional mechanism is attributed to the enhanced catalytic effect of partly contacted metals in our LbL bimetallic system; however, the enhanced mass transfer via the dual reaction pathway by both formate and CO as reactant is more considerable than the synergistic effect by bifunctional
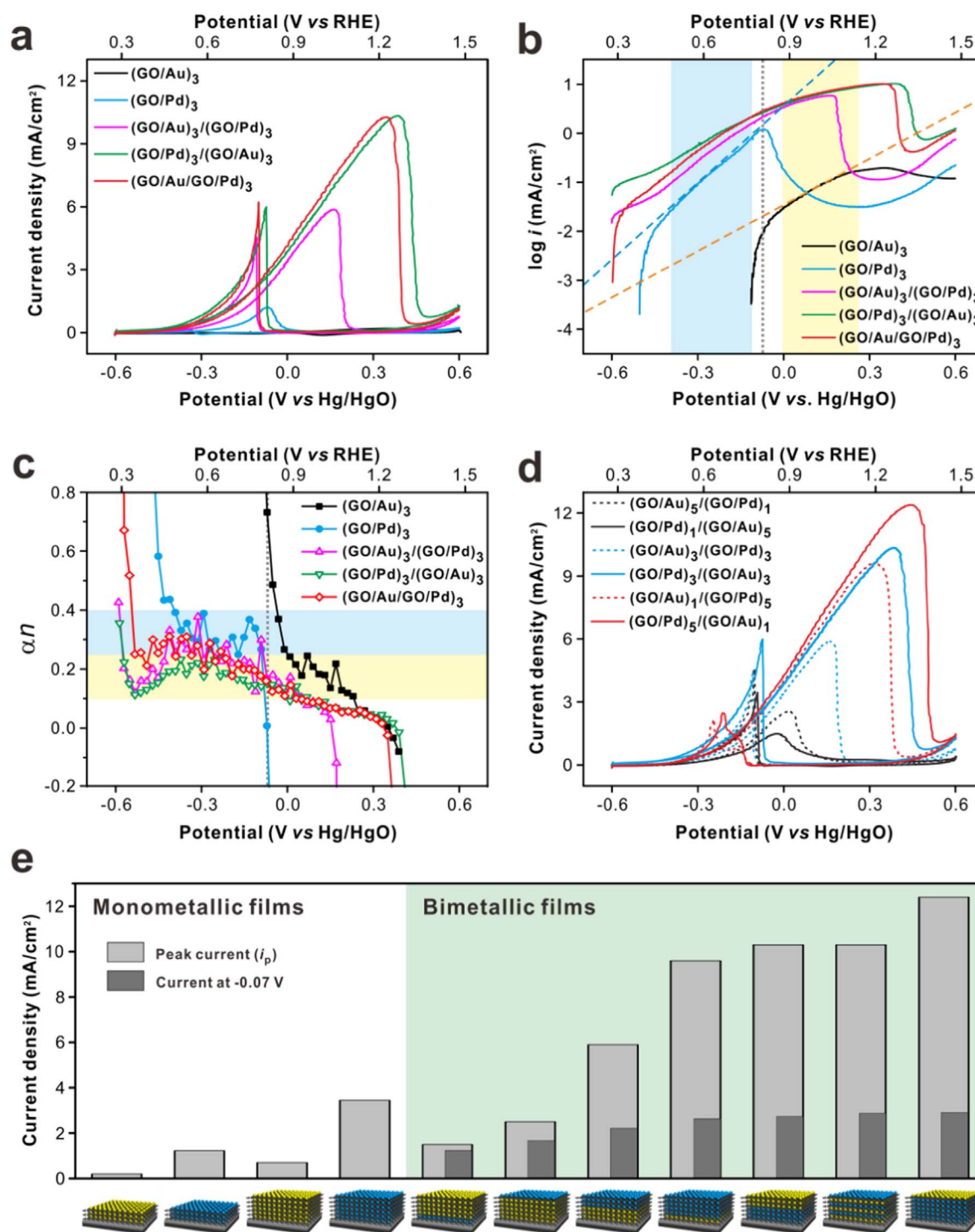
Fig. 4. Architectural effect in 3D multilayer electrode for methanol oxidation. (a) Cyclic voltammograms, (b) corresponding Tafel plots and (c) calculated αn, product of transfer coefficient (α) and number of electrons (n) of (GO/Au)$_3$, (GO/Pd)$_3$, (GO/Au)$_3$/(GO/Pd)$_3$, (GO/Pd)$_3$/(GO/Au)$_3$ and (GO/Au/GO/Pd)$_3$ multilayer films. (d) Cyclic voltammograms of (GO/Au)$_n$/(GO/Pd)$_{6-n}$ (dotted line), (GO/Pd)$_n$/(GO/Au)$_{6-n}$ (solid line) multilayer thin films (n =1, 3 and 5). (e) Comparison of electrochemical performance of all multilayer films with varying architecture toward MOR. Yellow and blue Tafel region corresponds to (GO/Au)$_n$ and (GO/Pd)$_n$, respectively. All measurements were measured in 0.10 M KOH with 1.0 M CH$_3$OH in a saturated N$_2$ at a scan rate of 20 mV s^{-1}.

mechanism.

We calculated a αn (α is the transfer coefficient and n is the number of electrons) of each LbL assembled electrode to further demonstrate the competitive mass and charge transfer mechanism analysis in the potential range from 0 to 0.25 V [47]. Negative αn value out of the range of 0–1 suggests that it does not follow the charge transfer limited system any longer. In range of each charge transfer limited system, (GO/Pd)$_3$ film, showing a lower Tafel slope, has higher αn values from

0.25 to 0.40 (blue region in Fig. 4c), while the (GO/Au)$_3$ films is lower in the range of 0.10–0.25 (yellow region in Fig. 4c). This observation commonly indicates that the first charge transfer in MOR is the rate-determining step [48,49]. Interestingly, all bimetallic hybrid electrodes showed continuous αn in the entire potential ranges, indicating that electrochemical reaction kinetics on bimetallic electrode follows the kinetics of monometallic electrode at each potential range. As a result, competitive mass and charge transfer between Pd and Au NPs in range
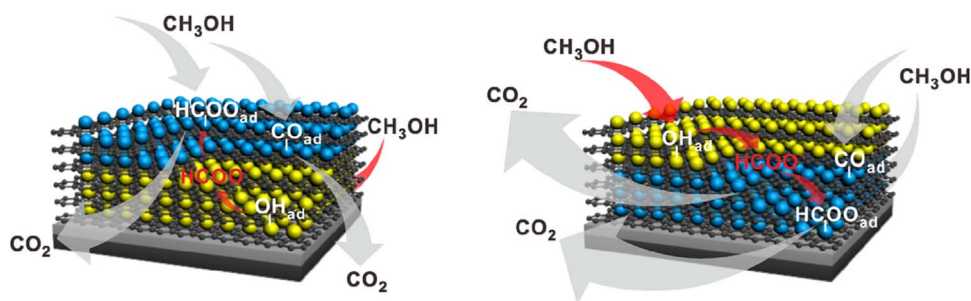
Scheme 1. Schematic representation of a controllable electrochemical mechanism between mass and charge transfer. Red and gray arrows indicate the diffusion flows on Au and Pd NPs, respectively in LbL assembled $(GO/Au)_3/(GO/Pd)_3$ and $(GO/Pd)_3/(GO/Au)_3$ multilayer thin films.

from 0 to 0.25 V was determined mainly by outer-layered metal NPs interfacing with the electrolytes.

Another factor that can influence on the electrocatalytic effect of 3D electrode with varying architectures can be the interface between outermost layer and electrolyte due to the morphological difference in LbL films (Fig. 3 and Fig. S10, S11 in the Supporting Information). The relatively rough surfaces in $(GO/Pd)_3/(GO/Au)_3$ multilayer not only provide more reaction sites of the electrode, but also enhance the mobility of methanol molecules into 3D electrode. To address the effect of morphological difference, electrochemical impedance spectroscopy (EIS) measurement was performed (Fig. S12 in the Supporting information). The charge transfer resistance (R_{CT}) values ascribed to semicircle of Nyquist plot of $(GO/Au)_3/(GO/Pd)_3$, $(GO/Pd)_3/(GO/Au)_3$ and $(GO/Au/GO/Pd)_3$ multilayer films correspond to 5346, 3899 and 2534 Ω at 0.35 V, respectively. The surface roughness can also enhance the interactions between NPs within the multilayer and electrolyte, eventually leading to a decrease in the contact resistance, R_{CT}. In addition, the more increment of the contact layers between Au and Pd NPs within fully co-assembled $(GO/Au/GO/Pd)_3$ multilayer could be attributed to a lower R_{CT} [50,51].

In order to further explore and feature the importance of LbL assembly in terms of controlling over the architecture of the electrode in achieving the best performance with a given set of component, we have fabricated co-assembled multilayers of Au and Pd NPs with GO in structures of $(GO/Au)_n/(GO/Pd)_{6-n}$ and $(GO/Pd)_n/(GO/Au)_{6-n}$ (n =1, 3 and 5) (Fig. 4d). In general, multilayers with outer Au NPs such as $(GO/Pd)_3/(GO/Au)_3$ and $(GO/Pd)_5/(GO/Au)_1$ showed a higher current density than those with outer-layered Pd NPs films with an exception of $(GO/Pd)_1/(GO/Au)_5$. The countertrend in $(GO/Pd)_1/(GO/Au)_5$ can also be speculated as follows: (i) the amount of single-layered Pd NPs as primary active sites than Au NPs is insufficient to the whole catalytic effect on LbL assembled 3D electrode; and (ii) the effect of outer-layered Pd NPs in direct contact with reactant methanol on topmost layer is more influential than that of aforementioned enhanced interaction in undermost layer by surface roughness of outer-layered Au NPs. Given the fact that the ECSA between same compositional films showed no significant difference (Fig. S13 in the Supporting information), this result also supports our explanation of the architectural effect by the enhanced mass transfer of outer-layered Au NPs as well as morphological difference, which affords more preferential interaction of electrode surface from electrolyte.

Finally, Fig. 4e and Table S1 summarize the electrochemical performance of all multilayer films with varying architecture toward MOR in this study. In monometallic films, Pd multilayer films showed the better electrocatalytic activity than Au multilayer films and electrocatalytic activity also increased with an increase in the number of bilayers. In bimetallic films, the anodic peak current increased highly with increasing the ratio of Pd as primary active sites and layering Au in outer-region of 3D multilayer films by the enhanced mass transfer. As a result, the $(GO/Pd)_5/(GO/Au)_1$ film showed the highest specific current (1105.6 mA/mg), considering the active mass of metal NPs based on QCM analysis as well as anodic peak current (12.4 mA/cm^2)

than any of the other multilayer films although commercial Pd/C catalyst showed a similar current density of 12.3 mA/cm^2 at a low peak potential of 0.08 V (Fig. S14 in the Supporting information). It is interesting that there is no distinct current density difference among bimetallic films at −0.07 V, which is a peak potential of $(GO/Pd)_3$ in spite of the enhanced catalytic activity than monometallic films, indicating the influential architecture effect in 3D electrode as well as synergetic effect of co-assembled Au and Pd NPs. It should be again emphasized that the highly tunable nature of LbL assembly only can afford the fabrication of the 3D electrode with an ultimate control over the structures to understand the electrochemical activity within the electrode and should be readily applied to the practical electrochemical electrodes.

4. Conclusions

In conclusion, we presented electrocatalytic thin films for methanol oxidation by adjusting the assembly sequence of LbL films. This 3D electrode prepared by the LbL assembly offers precise control not only over the thickness, but also the catalytic effect by changing the number of bilayers with two different NP catalysts on graphene supports. As a result, the heterogeneous $(GO/Au/GO/Pd)_n$ multilayers showed the highly enhanced catalytic effect for MOR than homogeneous $(GO/Au)_n$ and $(GO/Pd)_n$ multilayers because of not only the synergetic effect between Au and Pd NPs with the graphene sheets support, but also the oxidative removal effect of poisons on Pd NPs by neighboring Au NPs. Furthermore, owing to the tunable transition of thin firms from surface confined to diffusion limited process, LbL assembled electrode could provide a study model of mass and charge transfer system with respect to electrochemistry. The structural difference of Au and Pd NPs within the relative position of multilayer electrode affords highly tunable electrocatalytic activity, and thus confirming a novel versatility of LbL assembly to tailor the nanoarchitecture of hybrid electrodes.

Appendix B. Supporting information

Supplementary data associated with this article can be found in the online version at doi:10.1016/j.nanoen.2016.11.001.

References

[1] J.A. Turner, Science 285 (1999) 687–689.

[2] S. Chu, A. Majumdar, Nature 488 (2012) 294–303.

[3] D. Larcher, J.M. Tarascon, Nat. Chem. 7 (2015) 19–29.

[4] K. Ariga, Q.M. Ji, W. Nakanishi, J.P. Hill, M. Aono, Mater. Horiz. 2 (2015) 406–413.

[5] H. Abe, J. Liu, K. Ariga, Mater. Today 19 (2016) 12–18.

[6] J.J. Richardson, M. Bjornmalm, F. Caruso, Science 348 (2015) 2491.

[7] G. Decher, Science 277 (1997) 1232–1237.

[8] P.T. Hammond, Adv. Mater. 16 (2004) 1271–1293.

[9] C.Y. Jiang, V.V. Tsukruk, Adv. Mater. 18 (2006) 829–840.

[10] K. Ariga, J.B. Li, J.B. Fei, Q.M. Ji, J.P. Hill, Adv. Mater. 28 (2016) 1251–1286.

[11] J.F. Quinn, A.P.R. Johnston, G.K. Such, A.N. Zelikin, F. Caruso, Chem. Soc. Rev. 36 (2007) 707–718.

[12] E. Kharlampieva, V. Kozlovskaya, S.A. Sukhishvili, Adv. Mater. 21 (2009) 3053–3065.

[13] N.I. Kovtyukhova, P.J. Ollivier, B.R. Martin, T.E. Mallouk, S.A. Chizhik, E.V. Buzaneva, A.D. Gorchinskiy, Chem. Mater. 11 (1999) 771–778.

[14] H.L. Li, S.P. Pang, S. Wu, X.L. Feng, K. Mullen, C. Bubeck, J. Am. Chem. Soc. 133 (2011) 9423–9429.

[15] K. Jo, M. Gu, B.-S. Kim, Chem. Mater. 27 (2015) 7982–7989.

[16] M. Yang, Y. Hou, N.A. Kotov, Nano Today 7 (2012) 430–447.

[17] G. Rydzek, Q.M. Ji, M. Li, P. Schaaf, J.P. Hill, F. Boulmedais, K. Ariga, Nano Today 10 (2015) 138–167.

[18] Y. Choi, M. Gu, J. Park, H.-K. Song, B.-S. Kim, Adv. Energy Mater. 2 (2012) 1510–1518.

[19] Y.H. Chen, T. Chen, L. Dai, Adv. Mater. 27 (2015) 1053–1059.

[20] T. Lee, T. Yun, B. Park, B. Sharma, H.-K. Song, B.-S. Kim, J. Mater. Chem. 22 (2012) 21092–21099.

[21] M. Gu, J. Lee, Y. Kim, J.S. Kim, B.Y. Jang, K.T. Lee, B.-S. Kim, R.S.C. Adv, 4 (2014) 46940–46946.

[22] T.-K. Hong, D.W. Lee, H.J. Choi, H.S. Shin, B.-S. Kim, ACS Nano 4 (2010) 3861–3868.

[23] B.-S. Kim, S.W. Lee, H. Yoon, M.S. Strano, Y. Shao-Horn, P.T. Hammond, Chem. Mater. 22 (2010) 4791–4797.

[24] J. Hong, K. Char, B.-S. Kim, J. Phys. Chem. Lett. 1 (2010) 3442–3445.

[25] D.W. Lee, T.-K. Hong, D. Kang, J. Lee, M. Heo, J.Y. Kim, B.-S. Kim, H.S. Shin, J. Mater. Chem. 21 (2011) 3438–3442.

[26] S.H. Yang, T. Lee, E. Seo, E.H. Ko, I.S. Choi, B.-S. Kim, Macromol. Biosci. 12 (2012) 61–66.

[27] H.Hwang, P.Joo, M.S.Kang, G.Ahn, J.T.Han, B.-S.Kim, J.H.Cho, ACS Nano 62432-2440, 2012.

[28] P. Joo, B.J. Kim, E.K. Jeon, J.H. Cho, B.-S. Kim, Chem. Comm. 48 (2012) 10978–10980.

[29] S.-M. Kim, P. Joo, G. Ahn, I.H. Cho, D.H. Kim, W.K. Song, B.-S. Kim, M.-H. Yoon, J. Biomed. Nanotechnol. 9 (2013) 403–408.

[30] Y.K. Jung, T. Lee, E. Shin, B.S. Kim, Sci. Rep. 3 (2013) 3367.

[31] T. Lee, S.H. Min, M. Gu, Y.K. Jung, W. Lee, J.U. Lee, D.G. Seong, B.-S. Kim, Chem. Mater. 27 (2015) 3785–3796.

[32] M. Onda, Y. Lvov, K. Ariga, T. Kunitake, J. Ferment. Bioeng. 82 (1996) 502–506.

[33] W.S. Hummers, R.E. Offeman, J. Am. Chem. Soc. 80 (1958) (1339-1339).

[34] K. Jo, T. Lee, H.J. Choi, J.H. Park, D.J. Lee, D.W. Lee, B.-S. Kim, Langmuir 27 (2011) 2014–2018.

[35] D.I. Gittins, F. Caruso, Angew. Chem. Int. Ed. 40 (2001) 3001–3004.

[36] Y.-Y. Yang, J. Ren, H.-X. Zhang, Z.-Y. Zhou, S.-G. Sun, W.-B. Cai, Langmuir 29 (2013) 1709–1716.

[37] F. Gao, D.W. Goodman, Chem. Soc. Rev. 41 (2012) 8009–8020.

[38] Y.-H. Yang, L. Bolling, M.A. Priolo, J.C. Grunlan, Adv. Mater. 25 (2013) 503–508.

[39] L.R.F. Allen, J. Bard, Electrochemical Methods Fundamentals and Applications, 2nd edition ed., John Wiley & Sons, New York, 2000.

[40] L. Shao, J.W. Jeon, J.L. Lutkenhaus, Chem. Mater. 24 (2012) 181–189.

[41] C.H.A. Tsang, K.N. Hui, K.S. Hui, L. Ren, J. Mater. Chem. A 2 (2014) 17986–17993.

[42] X.G. Wang, B. Tang, X.B. Huang, Y. Ma, Z.H. Zhang, J. Alloy. Compd. 565 (2013) 120–126.

[43] P. Rodriguez, Y. Kwon, M.T.M. Koper, Nat. Chem. 4 (2012) 177–182.

[44] P. Lavalle, J.C. Voegel, D. Vautier, B. Senger, P. Schaaf, V. Ball, Adv. Mater. 23 (2011) 1191–1221.

[45] C. Picart, J. Mutterer, L. Richert, Y. Luo, G.D. Prestwich, P. Schaaf, J.C. Voegel, P. Lavalle, Proc. Natl. Acad. Sci. USA 99 (2002) 12531–12535.

[46] W.J. Huang, H.T. Wang, J.G. Zhou, J. Wang, P.N. Duchesne, D. Muir, P. Zhang, N. Han, F.P. Zhao, M. Zeng, J. Zhong, C.H. Jin, Y.G. Li, S.-T. Lee, H.J. Dai, Nat. Commun. 6 (2015) 10035.

[47] W.E. Mustain, J. Prakash, J. Power Sources 170 (2007) 28–37.

[48] A. Kowal, M. Li, M. Shao, K. Sasaki, M.B. Vukmirovic, J. Zhang, N.S. Marinkovic, P. Liu, A.I. Frenkel, R.R. Adzic, Nat. Mater. 8 (2009) 325–330.

[49] J. Luo, P.N. Njoki, Y. Lin, D. Mott, L.Y. Wang, C.J. Zhong, Langmuir 22 (2006) 2892–2898.

[50] F.-X. Xiao, J.W. Miao, B. Liu, J. Am. Chem. Soc. 136 (2014) 1559–1569.

[51] H.J. Wang, S. Ishihara, K. Ariga, Y. Yamauchi, J. Am. Chem. Soc. 134 (2012) 10819–10821.

Minsu Gu is a Ph.D. candidate under the supervision of Prof. Byeong-Su Kim in the Department of Energy Engineering at the Ulsan National Institute of Science and Technology (UNIST). He received B.S. degree in School of Nano-Bioscience and Chemical Engineering at UNIST in 2013. As a receipent of the Global Ph.D. Fellowship (GPF) from National Research Foundation of Korea, his current research interests are sysnthesis of energy-related carbon nanomaterials and electrochemistry of multilayer thin film electrodes for energy conversion and storage.

Dr. Byeong-Su Kim is an Associate Professor of Department of Chemistry at the Ulsan National Institute of Science and Technology (UNIST), Korea. He received Ph.D. in chemistry at the University of Minnesota in 2007. After a postdoctoral researches at MIT for two years, he started his independent career at UNIST since August 2009. His research and education program covers a broad span of macromolecular chemistry in the study of novel polymer and hybrid nanomaterials, including the molecular design and synthesis of self-assembled polymers, layer-by-layer assembly for functional thin films, and now expands to complex macromolecular systems such as carbon nanomaterials.